Energy & Environmental Science

PAPER

View Article Online
View Journal | View Issue

Cite this: *Energy Environ. Sci.*, 2019, **12**, 615

Extremely stable antimony–carbon composite anodes for potassium-ion batteries†

Jing Zheng,‡[ab] Yong Yang,‡[a] Xiulin Fan,[a] Guangbin Ji,[b] Xiao Ji,[a] Haiyang Wang,[a] Singyuk Hou,[a] Michael R. Zachariah*[ac] and Chunsheng Wang*[ac]

Received 27th September 2018,
Accepted 8th January 2019

DOI: 10.1039/c8ee02836b

rsc.li/ees

Potassium-ion batteries (PIBs) have been considered as promising alternatives to lithium-ion batteries due to potassium's high natural abundance of 2.09 wt% (*vs.* 0.0017 wt% for Li) and K/K^+ having a low redox potential of −2.93 V (*vs.* −2.71 V for Na/Na^+). However, PIB electrodes still suffer huge challenges due to the large K-ion radius and slow reaction dynamics. Herein, we report a high-capacity Sb@CSN composite anode with Sb nanoparticles uniformly encapsulated by a carbon sphere network (CSN) for PIBs. First-principles computations and electrochemical characterization confirm a reversible sequential phase transformation of KSb_2, KSb, K_5Sb_4, and K_3Sb during the potassiation/depotassiation process. In a concentrated 4 M KTFSI/EC + DEC electrolyte, the Sb@CSN anode delivers a high reversible capacity of 551 mA h g^{-1} at 100 mA g^{-1} after 100 cycles with an extremely slow capacity decay of only 0.06% per cycle from the 10th to 100th cycle; when at a high current density of 200 mA g^{-1}, the Sb@CSN anode still maintains a capacity of 504 mA h g^{-1} after 220 cycles. The Sb@CSN anodes demonstrate one of the best electrochemical performances for all K-ion battery anodes reported to date. The exceptional performance of Sb@CSN should be attributed to the efficient encapsulation of small Sb nanoparticles in the conductive carbon network as well as the formation of a robust KF-rich SEI layer on the Sb@CSN anode in the concentrated 4 M KTFSI/EC + DEC electrolyte.

Broader context

Recently, potassium-ion batteries (PIBs) have attracted increasing attention due to their low cost, abundant K resources, and low redox potential. However, conventional alloy PIB anodes still suffer from short cycle life due to huge volume changes during insertion/de-insertion of large-radius K ions. In this work, we significantly enhanced the cycling stability of Sb alloy anodes by dispersing nano-Sb into a porous sphere network (Sb@CSN) to mitigate the volume changes of Sb@CSN and using a highly concentrated 4 M KTFSI/EC + DEC electrolyte to form a robust KF-rich solid electrolyte interphase on Sb@CSN. The synergistic effect of the porous carbon substrate and robust SEI greatly enhance the electrochemical performance of the Sb@CSN anode. The synergistic design of K-ion battery alloy anodes will inspire battery scientists to deeply understand the fundamental electrochemistry in PIBs and will be very useful in developing the next generation of high-performance PIBs.

Introduction

With the continuously increasing consumption of traditional non-renewable energy sources along with severe global environmental issues, developing efficient and renewable energy storage technologies has never been more urgently required. Lithium-ion batteries (LIBs) as an efficient electrical energy storage technology have been successfully developed and widely used in various types of electronic devices and electric vehicles.[1,2] However, the broad utilization of LIBs in large-scale energy storage systems is still significantly hindered by the limited and unevenly distributed availability of Li in the earth's crust (0.0017 wt%).[3,4] In the past decades, many efforts have been devoted to developing alternative batteries using earth-abundant and cheap materials. Recently, sodium-ion batteries (SIBs) and potassium-ion batteries (PIBs) have received increasing attention because of their high abundance (2.36 and 2.09 wt% for Na

[a] Department of Chemical and Biomolecular Engineering University of Maryland, College Park, MD 20742, USA. E-mail: mrz@umd.edu, cswang@umd.edu; Fax: +1-301-314-9216; Tel: +1-301-405-4311, +1-301-405-0352
[b] College of Materials Science and Technology, Nanjing University of Aeronautics and Astronautics, Nanjing 210016, P. R. China
[c] Department of Chemistry and Biochemistry, University of Maryland, College Park, MD 20742, USA

† Electronic supplementary information (ESI) available. See DOI: 10.1039/c8ee02836b
‡ J. Z. and Y. Y. contributed equally to this work.

and K, respectively) and low cost.[5] Especially for PIBs, the lower redox potential (−2.93 V) for K/K^+ than for Na/Na^+ (−2.71 V *vs.* SHE) guarantees a higher operation voltage and higher energy density, making them a promising candidate for high-energy-density and low-cost electrical energy storage applications.

Significant advances have been achieved in developing high-performance PIB cathode materials such as amorphous $FePO_4$,[6] $FeSO_4F$,[7] Prussian blue,[8] Prussian green,[9] and organic materials.[10] The research on anode materials mainly focuses on carbonaceous materials, such as hard carbon,[11] soft carbon,[12] graphite,[13,14] and reduced graphene oxide.[15] However, these carbonaceous materials have a low capacity of less than 300 mA h g^{-1}. Metal anodes through an alloying/de-alloying reaction with K can provide a much higher specific capacity than that of intercalation type anodes.[16] As a result, adding metal into carbon materials can significantly enhance the capacity of carbonaceous materials. Recently, a Sn–carbon composite prepared by mechanical ball-milling of Sn powder with graphite was reported for PIBs. However, the capacity of the Sn–C composite anode quickly drops from 288 mA h g^{-1} after the 1st cycle to a low value of 150 mA h g^{-1} after the 30th cycle even at a low current density of 25 mA g^{-1}.[17] Such rapid capacity decay is caused by the large volume change during alloying/de-alloying processes, which leads to obvious electrical disconnection between the electrode material and current collector.[18] Although encapsulation of Sn nanoparticles in a carbon skeleton,[19] mesoporous nanostructured carbon,[20] or nanocrystalline materials[21] can mitigate the damage from volume expansion/contraction during cycling, the capacity of Sn@C anodes still declines during the charge/discharge cycles due to high mobility of Sn nanoparticles. Alternatively, antimony (Sb) with a low mobility has been investigated for PIB anodes. As in Li-ion and Na-ion batteries,[22,23] Sb can also form K_3Sb[24] by reacting with K. However, the Sb-based anode prepared by simple ball-milling of a mixture of carbon black and "bulk" antimony powder can only provide a capacity of 250 mA h g^{-1} after 50 cycles, similar to the Sn@C anode in PIBs.[25] Furthermore, electrolytes are also critical for stabilizing PIB anodes because the nature of the solid electrolyte interphase (SEI) layer on the anode significantly affects the cycling performance of PIBs.[26] However, to our best of knowledge, only limited studies on SEI design *via* rational electrolyte regulation have been reported.[27,28] Therefore, in order to achieve a high capacity and excellent cycle stability for a Sb-based K storage process, nanostructure improvements as well as electrolyte design should be considered simultaneously.

Herein, a novel type of Sb-based composite is prepared *via* a scalable electrospray-assisted strategy. This approach enables Sb nanoparticles to be uniformly encapsulated by an interconnecting carbon sphere network (Sb@CSN), which not only works as a buffering matrix to mitigate the deleterious mechanical damage from the large volume changes during alloying/de-alloying cycling, but also acts as a highly conductive framework for fast electron transport. More importantly, we also regulate the components of ester-based electrolytes to promote the formation of a KF-rich SEI layer on the Sb@CSN anode. Surprisingly, the Sb@CSN composite in the optimized 4 M KTFSI/EC + DEC electrolyte delivers an excellent reversible capacity of 551 mA h g^{-1} at 100 mA g^{-1} after 100 cycles with a low capacity decay of 0.06% per cycle from the 10th to 100th cycle and 504 mA h g^{-1} even at a high current density of 200 mA g^{-1} after 220 cycles. Sb@CSN composite anodes also show an excellent rate performance by providing a high capacity of 589 mA h g^{-1} at 50 mA g^{-1} and still maintaining 530 mA h g^{-1} even at 200 mA g^{-1}. These outstanding performances should be attributed to the novel nanostructure of Sb nanoparticles uniformly encapsulated in the conductive carbon network and the formation of a more stable and robust KF-rich SEI layer on Sb@CSN in the optimizd 4 M KTFSI/EC + DEC electrolyte. To our best knowledge, the Sb@CSN composites in our work show one of the highest capacities and the longest cycle life for all reported PIBs anodes to date.

Result and discussion

Sb@CSN materials were synthesized using a scalable electrospray-assisted strategy, as illustrated in Scheme 1. Under the controllable high-voltage electrostatic field between the needle and the substrate collector, the precursor solution containing polyacrylonitrile (PAN) and $SbCl_3$ was nebulized to generate high concentrations of highly charged microdroplets when dried in free flight, which served as the primary building blocks for porous 3D network construction. The formed PAN nanospheres with evenly-distributed $SbCl_3$ (marked as $SbCl_3$/PAN) were collected from the substrate and then thermally stabilized and reduced to generate uniform metal Sb nanoparticles which were well confined in an *in situ* formed carbon sphere network (CSN) to obtain the Sb@CSN material.

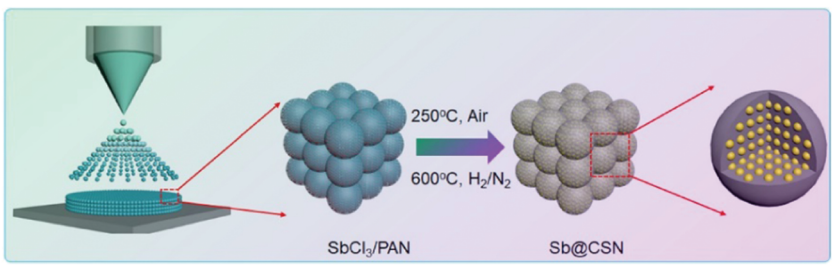

Scheme 1 Schematic illustration of the electrospray-assisted strategy for fabricating the Sb@CSN material.

Fig. 1 demonstrates the structure and morphology of the Sb@CSN composite material revealed by XRD, TG-DSC, Raman, and SEM analysis. As shown in Fig. 1a, the XRD pattern of the Sb@CSN material is consistent with hexagonal Sb (JCPDS no. 35-0732), without any other phases or impurities, indicating that Sb^{3+} was reduced completely to metallic Sb during the synthesis process. Using the Scherrer equation with the (012) peaks of Sb, the average size of Sb crystallites was calculated at around 18 nm. On the other side, the Raman spectrum was used to reveal the structure properties of the carbon in Sb@CSN composites. The Raman spectrum in Fig. 1b shows three bands at 1350, 1597, and 2880 cm^{-1}, corresponding to D, G and 2D bands; moreover, the intensity ratio between the G and D band (I_G/I_D) is 1.02, suggesting a high degree of graphitization for the carbon in Sb@CSN, which should offer better electro-conductivity.[29] To evaluate the content of Sb in the prepared Sb@CSN material, TG-DSC analysis was carried out in air from room temperature to 1000 °C, as displayed in Fig. 1c. The slight weight loss at around 100 °C resulted from adsorbed solvent evaporation; the main weight loss at around 500 °C is due to carbon oxidation. According to the oxygen–antimony binary phase diagram (Fig. S1a, ESI†), a small peak in the DCS curve at around 590 °C is attributed to the oxidation of Sb nanoparticles to form Sb_2O_4.[30] As a result, the mass loading of Sb for the prepared Sb@CSN material can be calculated at around 37.8 wt%.

The morphology of the $SbCl_3$/PAN precursor and Sb@CSN before and after heat treatment is shown in Fig. 1d–f and g–i, respectively. The as-prepared $SbCl_3$/PAN precursor in Fig. 1d–f demonstrates uniform spheres which interconnect to form a three-dimensional (3D) network. Notably, these spheres have a crumpled surface, probably formed by the capillary compression during the solvent evaporation from the aerosol droplets.[31] This crumpled surface microstructure can be very beneficial for boosting the surface area of the carbon network. After carbonization, the obtained Sb@CSN maintains a similar microstructure and morphology, indicating that the unique structure of the prepared material can be maintained after the heat treatment. Fig. 1g–i illustrates the interconnection between each primary carbon sphere with embedded secondary Sb nanoparticles (Fig. S1b and c, ESI†), which enables the continuous 3D conductive network to provide a fast electronic and ionic transfer path and effectively accommodate the volume changes.

The microstructure and morphology of Sb@CSN were also examined by TEM analysis, as shown in Fig. 2. Fig. 2a represents a schematic illustration of uniform Sb nanoparticles confined in a carbon sphere. The corresponding TEM image in Fig. 2b indicates that the Sb nanoparticles are well-encapsulated and uniformly distributed in the carbon sphere. The size distribution curve in Fig. 2c indicates a relatively narrow size distribution for Sb nanoparticles in the prepared Sb@CSN material, with an average size of 14 nm and a standard deviation of 3.4 nm, which is consistent with the XRD results. The HRTEM image shown in Fig. 2d suggests that the Sb nanoparticle has a good crystalline structure, confirmed by the 3.1 Å distance of lattice fringes

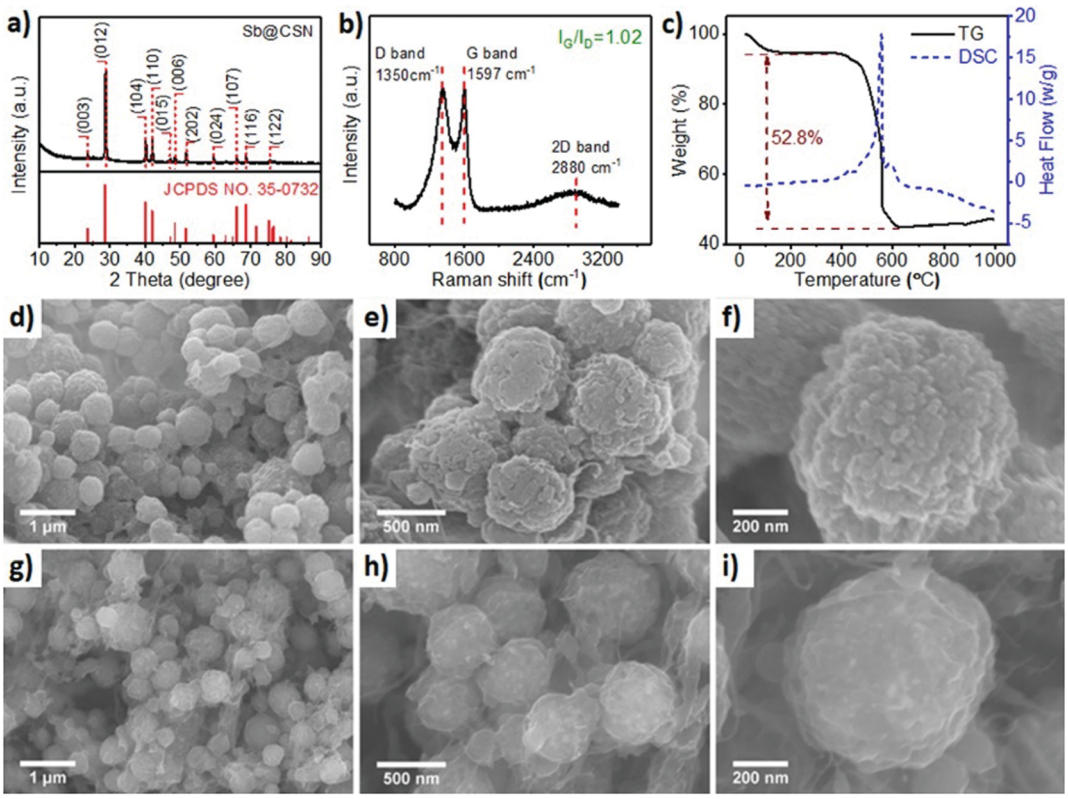

Fig. 1 (a) XRD pattern, (b) Raman spectra, and (c) TG-DSC curves for the Sb@CSN material; SEM images of the (d–f) as-prepared $SbCl_3$/PAN precursor and (g–i) Sb@CSN composite.

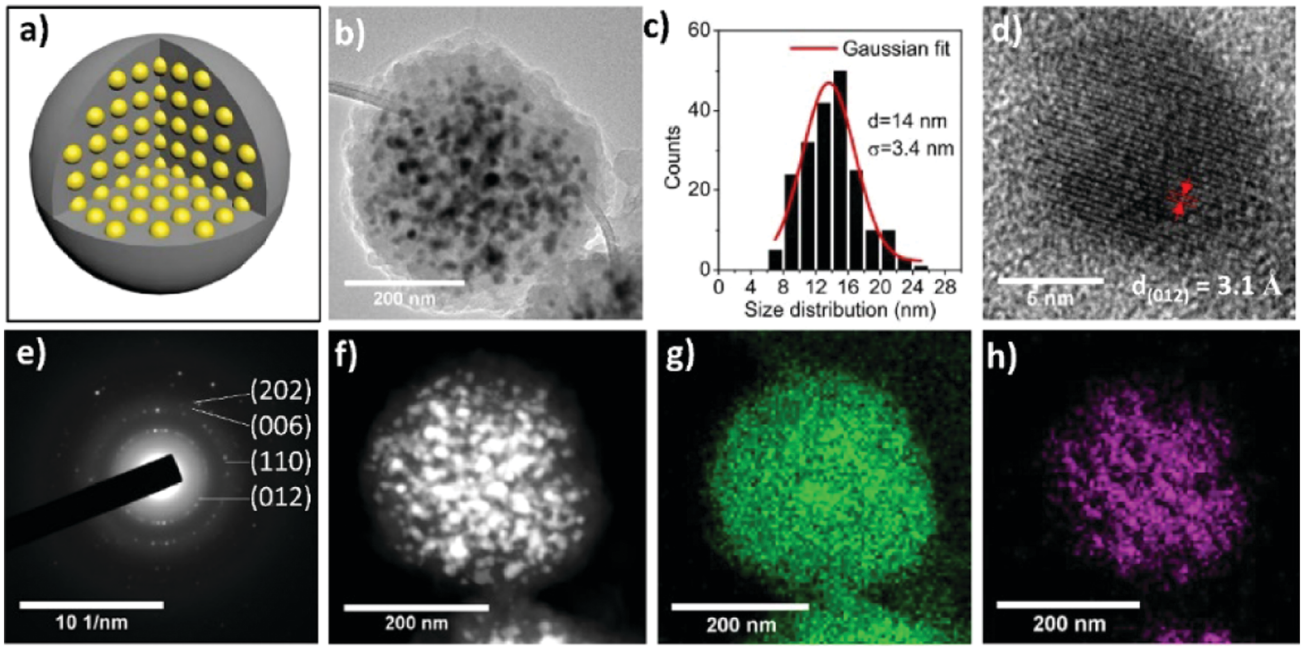

Fig. 2 (a) Schematic illustration of uniform Sb nanoparticles confined in a carbon sphere (Sb@CSN); (b) TEM image of an individual Sb@CSN sphere and (c) corresponding size distribution curve of Sb nanoparticles from image (b); (d) HRTEM image, (e) selected-area electron diffraction pattern, and (f–h) EDS images for one individual Sb@CSN sphere, (g) for C and (h) for the Sb element.

corresponding to the (012) plane of the metallic Sb. The selected-area electron diffraction pattern (SAD) in Fig. 2e exhibits the typical SAD pattern of metallic Sb. The lack of diffraction rings corresponding to Sb_2O_4 suggests that the carbon matrix serves as an effective barrier to prevent the Sb nanoparticles from oxidizing. The element mapping images in Fig. 2f–h suggest a uniform distribution of Sb nanoparticles in the carbon sphere matrix.

According to the potassium–antimony binary phase diagram (Fig. S2a, ESI†), there are four intermediate phases going from KSb_2 to KSb, K_5Sb_4 and then K_3Sb with the increase of the K content, and the corresponding crystalline structures are exhibited in Fig. 3a. The equilibrium potential for the reaction process of K with Sb was obtained using first-principles computations based on density functional theory (DFT). As can be seen from Fig. 3b, the thermodynamic equilibrium potentials of KSb_2 and KSb are 0.89 V and 0.849 V, respectively. Similarly, the two adjacent equilibrium potentials of K_5Sb_4 and K_3Sb are 0.439 V and 0.398 V, respectively. The K concentration in K_xSb interphases corresponds to x = 0.5, 1.0, 1.25, and 3.0 with a theoretical capacity of 108, 216, 270, and 660 mA h g^{-1}, occupying total capacity percentages of 16.4%, 16.4%, 8.2%, and 59.1%, respectively. Furthermore, two prominent potential platforms can be clearly found in the calculated potential profile, corresponding to the equilibrium potentials of the above-mentioned interphases. A dramatic potential drop from around 0.9 V to 0.4 V is seen when the capacity exceeds 216 mA h g^{-1}; subsequently, the potential profile slowly decreases from 0.439 V to 0.398 V, with the formation of K_3Sb.

The electrochemical behavior of the Sb@CSN anode was evaluated using cyclic voltammetry (CV) at a scan rate of 0.05 mV s^{-1} in coin cells using K as the counter electrode and 4 M KTFSI/EC + DEC (abbreviated as "4 M KTFSI") as the electrolyte. As displayed in Fig. 3c, two pairs of redox peaks at approximate 0.4 V and 0.9 V potentials can be observed in the CV curve during the alloying/de-alloying process, consistent with the calculated intermediate K_xSb phases located at around 0.9 V and 0.4 V in Fig. 3b. The alloying peak located at around 0.78 V in the potassiation process should be attributed to the stepwise alloying reaction of Sb to form KSb_2/KSb. Furthermore, the similar equilibrium reaction voltage between these two intermediates leads to an appearance of the overlap broad peak at 0.78 V. Another reduction peak centered at about 0.23 V is also an overlap broad peak, which resulted from the approximate formation voltage for both K^+ insertion in C and the step formation of K_5Sb_4 and K_3Sb alloys.[32] Based on the potential–capacity curve in Fig. 3b, the formation of K_3Sb occupied a large proportion of the theoretical capacity (58.5%), which is the reason why the peak at 0.23 V is larger than that of 0.78 V. The peak voltages both at 0.78 V and 0.23 V are slightly lower than that of the corresponding value from theoretical calculations, which is primarily due to the overpotential. In the reverse anodic scan, there is a distinct anodic peak at 0.64 V and a minor oxidation peak at 1.12 V, which is due to the extraction reaction of K during the depotassiation reaction. In similar manner, the peaks of K_3Sb and K_5Sb_4 overlap with each other to form a new broad apparent peak at 0.64 V but an inconspicuous peak of KSb and KSb_2 at 1.12 V. In the same situation of the overpotential, these oxidation peaks gradually shifted to higher potentials when compared with the theoretical values. Owing to SEI film formation during the first cathodic scan, a lower current peak after the initial cycle is observed, slightly distinguished

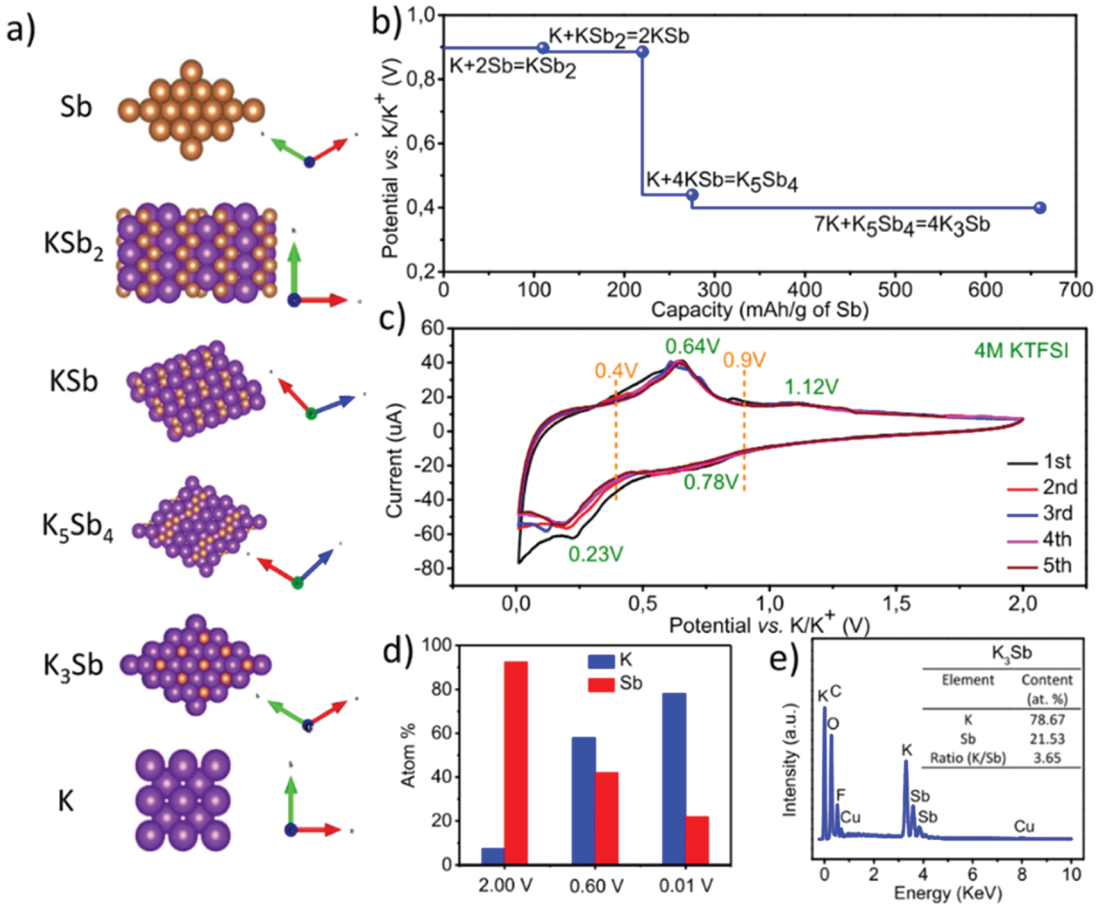

Fig. 3 (a) Crystal structure of K and stages of the structure evolution from Sb to K_3Sb during the potassiation process; (b) DFT calculated equilibrium voltages (*vs.* K/K^+) for the potassiation process; (c) CV curves for the Sb@CSN electrode at a scan rate of 0.05 mV s^{-1}; (d) relative atom% of K and Sb from EDS with different discharge cut-off voltages; (e) EDS element analysis for K_3Sb with a discharge cut-off voltage of 0.01 V. (Cells from (c–e) are all in 4 M KTFSI electrolyte.)

from subsequent cycles where the SEI layer has already formed.[33] However, after the second and subsequent reduction/oxidation scans, the CV curves remain stable in their shapes and current intensities. Therefore, the CV curves demonstrate that the Sb@CSN material can perform a reversible alloying/de-alloying reaction with K in a potential region of 0.01–2.0 V.

Energy dispersive spectroscopy (EDS) elemental mapping was carried out to investigate the chemical composition of the formed interphases during the charging/discharging process. Fig. 3d shows the atomic percentages of K/Sb from the Sb@CSN electrode taken at different cut-off voltages (2.0, 0.6, and 0.01 V) during the 5th discharge process. The ratio of K/Sb can provide insight into the composition of the alloy interphase at each cut-off voltage. Obviously, along with the increasing discharge depth from 2 V to 0.01 V, the atomic ratio of K to Sb increases, indicating a deeper K alloying reaction with Sb. Notably, the ratio of K/Sb maintains a constant value of 3.65 in EDS elemental mapping when the cut-off voltage is 0.01 V (Fig. 3e), slightly higher than that of K_3Sb, which is probably attributed to the residual potassium salt from the electrolyte. Furthermore, as shown in Fig. S2b–f (ESI†), the elements of C, K and Sb have an even distribution on a nanometer scale within the Sb@CSN electrode even at the highest discharge depth of 0.01 V.

Fig. 4a shows the galvanostatic charge/discharge behavior of Sb@CSN in the 4 M KTFSI concentrated electrolyte at a low current density of 50 mA g^{-1} in the second cycle after the formation of the SEI. The mass capacities of Sb were calculated by subtracting the corresponding capacity contributed by the CSN. The CSN material without any Sb provides 110 to 180 mA h g^{-1} capacity at a current of 50–200 mA g^{-1}, as shown in Fig. S3 (ESI†). In this work, evidently, the voltage profile exhibits two prominent discharge voltage plateaus, located at about 0.78 V ending with a capacity of about 216 mA h g^{-1} and 0.23 V ending with ~646 mA h g^{-1}, corresponding to the potassiation reaction of Sb to KSb_2/KSb and K_5Sb_4/K_3Sb, respectively, and two charge platforms were found at 0.64 V and 1.12 V, which can be attributed to the extraction reaction of K from K_3Sb to Sb. Both the platform voltages and intensity of these two discharging/charging plateaus are in good agreement with the above-mentioned CV experimental results and calculated voltage profile. Fig. S4 (ESI†) shows the first galvanostatic charge–discharge profile of the Sb@CSN anode for the same current and electrolyte. In the first charge/discharge cycle, the Sb@CSN

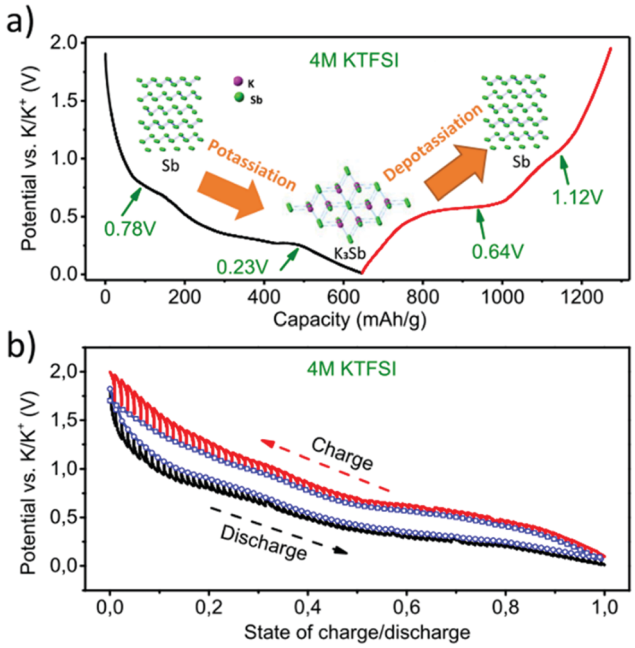

Fig. 4 Electrochemical K storage properties for Sb@CSN in the 4 M KTFSI electrolyte. (a) Typical 2nd charge/discharge profile at 50 mA g^{-1}; (b) quasi-equilibrium voltage profile from the galvanostatic intermittent titration technique (GITT) at 100 mA g^{-1}.

anode delivered an initial alloying and de-alloying capacity of 1049 and 640 mA h g^{-1}, respectively, leading to a low coulombic efficiency (CE) of 61%. It can be ascribed to the formation reaction of the irreversible SEI layer on the surface of the electrode, which is consistent with the reported results of the Sb anode.[34] The quasi-thermodynamic equilibrium potential and K^+ diffusivity coefficient for Sb@CSN were measured using the galvanostatic intermittent titration technique (GITT) after 10 charge/discharge activation cycles, as indicated in Fig. 4b.[35] The cell was discharged/charged at a current pulse of 100 mA g^{-1} for a duration period of 20 min, followed by an open-circuit stand for 120 min to allow full relaxation back to its quasi-equilibrium potential. The quasi-equilibrium potential at different normalized K insertion/extraction levels is indicated by the blue dotted lines in the GITT curves. The potential difference between the end of charge/discharge and the end of the relaxation period represents the overpotential in the corresponding depotassiation/potassiation stage.[36] It can be observed that the overpotential for the depotassiation and potassiation process is as low as 0.15 V even at a high current of 100 mA g^{-1}, suggesting fast K^+ diffusion in the Sb@CSN material. Furthermore, the four successive GITT curves displayed in Fig. S5 (ESI†) demonstrated a reversible potassiation/depotassiation process with a repeatable overpotential as low as 0.15 V. These results strongly suggest that fast and reversible depotassiation/potassiation dynamics can be achieved for the prepared Sb@CSN material in the 4 M KTFSI electrolyte.

The cycle stability for the as-prepared Sb@CSN material was investigated in 1 M KTFSI/EC + DEC (abbreviated as "1 M KTFSI") dilute and 4 M KTFSI concentrated electrolytes, respectively. Fig. 5a presents the cycling stability and its corresponding CE during 100 charge/discharge cycles at 100 mA g^{-1} in 1 M and 4 M KTFSI electrolytes. Specifically, the capacity of the Sb@CSN anode in the 4 M KTFSI electrolyte exhibits exceptional reversibility and cycling stability, maintaining a stable capacity of 551 mA h g^{-1} after 100 cycles with a high average CE of >98% and a low capacity decay of 5.3% from the 10th to 100th cycle; while the capacity of the Sb@CSN material in the 1 M KTFSI electrolyte fades rapidly, with only 286 mA h g^{-1} left after the 100th cycle with a fluctuant average CE of 95%. Similarly, the capacity of the Sb@CSN anode in the common dilute 1 M KPF_6/EC + DEC electrolyte also delivers a rapid capacity loss, with a discharge capacity of 603 mA h g^{-1} after the 2nd cycle but only 256 mA h g^{-1} after 100 cycles, as indicated in Fig. S6 (ESI†), suggesting the significant improvement of the electrochemical K-storage performance of the Sb@CSN material by electrolyte optimization. Furthermore, the cycled Sb@CSN material also maintained a completely spherical morphology with uniform Sb nanoparticles encapsulated in a well-defined manner in the carbon sphere (Fig. S7, ESI†), indicating excellent structure stability and efficient relief of the huge volume change during electrochemical reactions. These advanced properties should be ascribed to the well-designed carbon sphere matrix which can not only provide more space from its porous structure and defects to accommodate the volume change,[37] but also possesses excellent flexibility and good adhesion to Sb nanoparticles to remarkably stabilize the Sb nanoparticles and reduce the strain during the volume change process, protecting the CSN from cracking.[38]

The impedance changes during charge/discharge cycles were measured using electrochemical impedance spectroscopy (EIS). Fig. S8 (ESI†) shows the impedance of Sb@CSN before and after 100 cycles in 1 M and 4 M KTFSI electrolytes. It can be observed that the initial charge transfer resistance in the 4 M KTFSI electrolyte is higher than that in the 1 M KTFSI electrolyte, which can be attributed to the lower wettability of the concentrated 4 M electrolyte on the Sb@CSN electrodes due to the higher viscosity of the 4 M concentrated electrolyte than that of the 1 M dilute electrolyte. After 100 charge/discharge cycles, only a small increase in the electron-involving reaction impedance is observed for Sb@CSN in the 4 M KTFSI electrolyte, while a large electron-involving reaction impedance increase is demonstrated in the 1 M KTFSI electrolyte. This result can be probably attributed to the formation of a thinner solid electrolyte interface (SEI) layer on Sb@CSN in the 4 M electrolyte.

The long-term cycling stability of the Sb@CSN composite in the 4 M KTFSI electrolyte at a high current density of 200 mA g^{-1} was also evaluated. As shown in Fig. 5b and c, Sb@CSN at 200 mA g^{-1} in 4 M KTFSI still provides a high discharge capacity of 626 mA h g^{-1} after the 2nd cycle, which is very close to its theoretical capacity of 660 mA h g^{-1} (corresponding to the formation of K_3Sb). The capacity slightly decreases in the initial 10 cycles and then stabilizes at 504 mA h g^{-1} after 200 cycles. Correspondingly, the CE increases in the first 10 cycles and then approaches a consistent value of 98%. These results manifest a reversible alloying–dealloying process between the

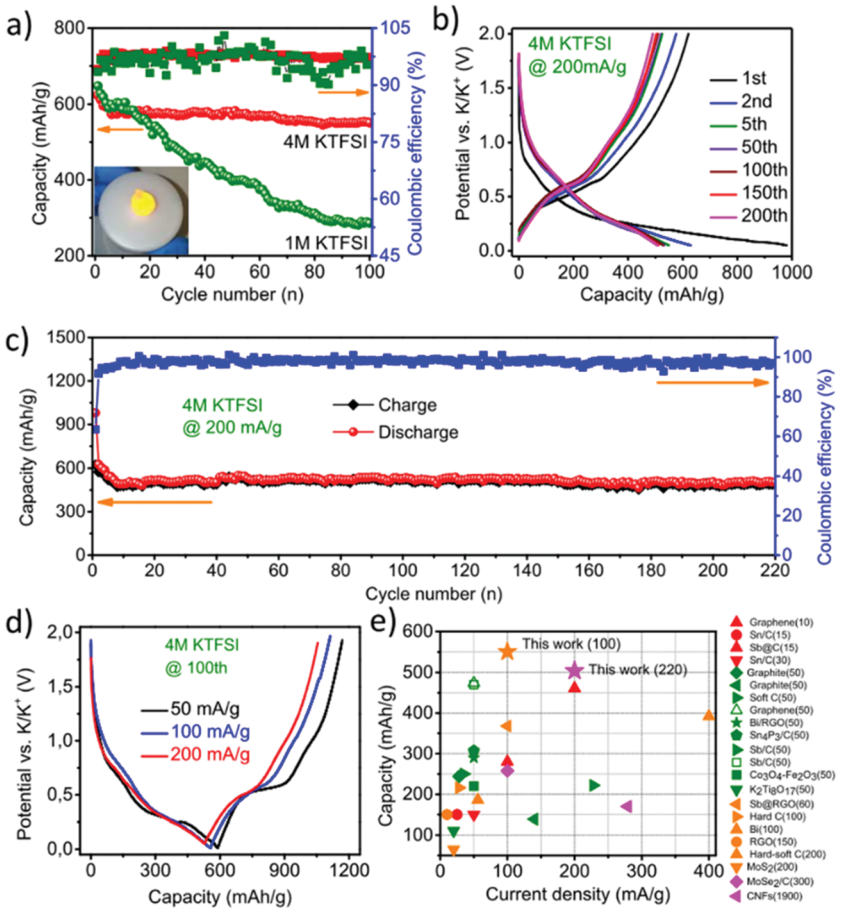

Fig. 5 Electrochemical performance for the Sb@CSN anode: (a) cycling performance at 100 mA g^{-1} in 1 M KTFSI and 4 M KTFSI electrolytes (inset: lighting an electronic candle with a coin cell in the 4 M KTFSI electrolyte after 100 cycles); (b) charge/discharge curves and (c) corresponding cycling performance at 200 mA g^{-1} in the 4 M KTFSI electrolyte; (d) the 50th charge/discharge curve under various current densities from 50 to 200 mA g^{-1}; (e) capacity comparison of the Sb@CSN anode with previous reported anodes in PIBs, the numbers in brackets are the cycle numbers, and the color code represents the cycling number range: red is <50 cycles, olive is 50 cycles, orange is 50 to 200 cycles, magenta is >200 cycles.

formation of Sb and K_3Sb even at such a high current density. Furthermore, Fig. 5d displays the charge–discharge profiles at various current densities after 50 cycles. The charge/discharge capacity only slightly decreases when increasing the current density from 50 to 100 and then 200 mA g^{-1}, along with a slight capacity decay from 589 mA h g^{-1} to 566 mA h g^{-1} and then 530 mA h g^{-1}, respectively, which indicates excellent rate capability for the unique nanostructured Sb@CSN in the 4 M KTFSI electrolyte. Moreover, the voltage plateaus at various current densities show small differences, indicating only minor electrochemical polarization augmentation when increasing to a higher current.

Fig. 5e and Table S1 (ESI†) compare the electrochemical performance of Sb@CSN in the 4 M KTFSI electrolyte with reported K-ion battery anodes, including carbon-based anodes, metal alloy anodes, and metal oxide (sulfide) anodes. It can be found that Sb@CSN can achieve a high specific capacity of 551 mA h g^{-1} at 100 mA g^{-1} after 100 cycles with a capacity decay of 0.06% per cycle from the 10th to 100th cycle and 504 mA h g^{-1} at a high current density of 200 mA g^{-1} even after 220 cycles, which are much better than all reported K-ion battery anodes. Such excellent performance should be attributed to (i) the carbon sphere network which not only acts as an efficient conductive skeleton but also as a buffer for huge volume expansion of Sb nanoparticles during the alloying/de-alloying reaction process, (ii) the small Sb crystallite with an average size of 14 nm which benefits the decrease of the K^+ diffusion distance, and (iii) the concentrated 4 M KTFSI electrolyte employed here which can promote the formation of a robust SEI to obtain good reversibility for the alloying/de-alloying reaction process.

The SEI compositions formed on Sb@CSN electrodes in 4 M KTFSI and 1 M KTFSI electrolytes were analyzed using X-ray photoelectron spectroscopy (XPS) coupled with the Ar^+ etching technique. As demonstrated in Fig. 6a and b, the signal of the Sb element at the etching time demonstrated that the SEI in the 4 M KTFSI electrolyte is thinner than that in the 1 M KTFSI electrolyte (Table S2, ESI†). Moreover, the SEI layer formed in the 4 M KTFSI electrolyte delivers an obviously lower C at% and higher F at% than that formed in the 1 M KTFSI electrolyte, indicating that a F-rich and inorganic-dominated SEI layer is preferentially formed in the 4 M concentrated electrolyte.[39] Fig. 6c and d show the high resolution F1s XPS spectra for

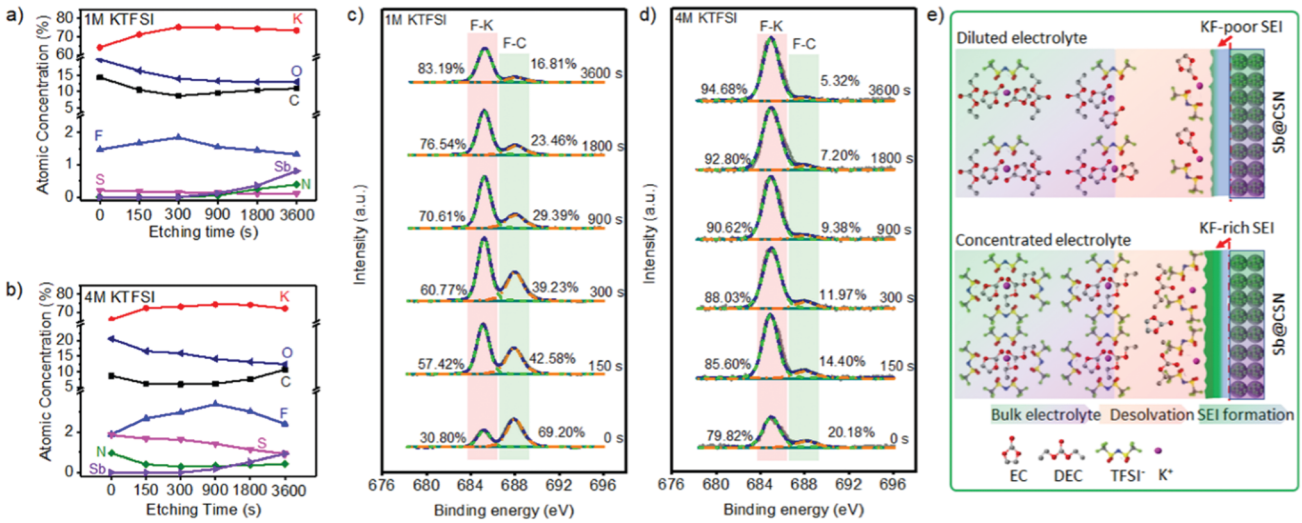

Fig. 6 (a and b) Atomic percentage concentrations of different elements with increasing etching time and (c and d) corresponding high-resolution F1s XPS spectra for the Sb@CSN electrode in (a and c) 1 M KTFSI and (b and d) 4 M KTFSI electrolyte; (e) illustration of the influence of dilute and concentrated electrolytes on the formation of the SEI layer.

the electrode surface in 1 M KTFSI and 4 M KTFSI electrolytes, respectively. Two main signal peaks centered at 685.0 and 688.1 eV in both electrolytes are assigned to F–K bonds and F–C bonds, respectively.[40] It can be found that at the outside surface (corresponding to an etching time of 0 s) of the Sb@CSN electrode in the 1 M KTFSI electrolyte, 69.20 at% of the F element exists as organic F–C bonds, suggesting an organic property of this surface. With the increasing etching time, the content of F–C bonds decreases gradually to 16.81 at%, indicating the changes of SEI composition from an organic sublayer to an organic–inorganic hybrid sublayer. By contrast, the content of F–C bonds in the SEI layer formed in the 4 M KTFSI electrolyte is distinctly lower than that formed in the 1 M KTFSI electrolyte at all the etching times, resulting in a F–K dominated bonding property for the F element in the SEI layer. These results suggest a more inorganic SEI layer with abundant KF phase was formed in the concentrated 4 M KTFSI electrolyte, well consistent with the previous report.[27] The highly concentrated KTFSI electrolyte can weaken the solvent reduction and lead to the reduction of KTFSI to mainly induce the formation of a KF-rich SEI.

As demonstrated in Fig. 6e, during the formation of the SEI layer, K^+, $TFSI^-$ and solvent molecules should first reach the electrode/electrolyte interface and then react irreversibly. It's much easier for the concentrated electrolyte to provide more $TFSI^-$ ions with abundant F element to reach the interface and then participate the SEI formation reaction in a faster kinetic way than in the 1 M diluted electrolyte. Accompanied by the condition of concentrated K^+, a denser and thinner KF-rich SEI layer was preferentially formed in the 4 M KTFSI electrolyte. Such a robust KF-rich SEI layer can not only protect the active materials from further reacting with the electrolyte, but also accommodate the volume change of Sb@CSN, thus leading to excellent K-storage performance for such a material. In addition, the highly concentrated KTFSI also reduced the solubility of KF in the electrolyte, further stabilizing the KF-rich SEI for excellent long-term cycling properties.

The highly concentrated electrolyte can also reduce the flammability. The flammability of electrolytes was evaluated by soaking a piece of glass fiber membrane in 0.5 mL electrolyte and then immediately igniting it with a butane lighter, as illustrated in Fig. S9 (ESI†). The flame for the 4 M KTFSI electrolyte is much smaller and darker than that of the dilute electrolyte and the same concentrated 4 M $KClO_4$ electrolyte. After the combustion, the glass fiber in the 4 M KTFSI electrolyte is black due to the fire retardation and incomplete combustion resulting from the stable and highly concentrated KTFSI salt. By contrast, it is white for the dilute electrolyte, indicating the complete combustion of the electrolyte. For the 4 M $KClO_4$ electrolyte, an obvious explosion can be observed due to the strong oxidization property of $KClO_4$. Therefore, the highly concentrated 4 M KTSFI electrolyte is suitable for highly secure batteries with less fire-severity and lower fire-catching properties.

Conclusion

In summary, a Sb@CSN composite anode with evenly-distributed and small Sb nanoparticles confined in a carbon sphere network has been successfully prepared for K-ion battery anodes *via* a unique electrospray-assisted strategy. The Sb@CSN anode in the concentrated 4 M KTFSI electrolyte shows a high reversible capacity of 551 mA h g^{-1} at 100 mA g^{-1} after 100 cycles with a capacity decay of 0.06% per cycle from the 10th to 100th cycle and 504 mA h g^{-1} after 220 cycles even at a high current density of 200 mA g^{-1}. It also shows excellent rate performance by providing 589 mA h g^{-1} at 50 mA g^{-1} and 530 mA h g^{-1} at 200 mA g^{-1}. Such a unique material in this concentrated electrolyte demonstrates one of the best capacity performances among all K-ion battery anode materials. These excellent K-storage performances

should be ascribed to the formation of a stable and robust KF-rich SEI layer along with the novel nanostructure of Sb nanoparticles uniformly encapsulated in the conductive carbon network. These discoveries provide valuable guidance for rationally developing advanced alloy-based electrode materials for high-performance PIB applications.

Conflicts of interest

The authors declare no competing financial interest.

Acknowledgements

This work was supported by the US National Science Foundation Award No. 1438198. We acknowledge the support of the Maryland NanoCenter and its AIM Lab. The AIM Lab is supported in part by the NSF as a MRSEC Shared Experimental Facility. Y. Y., H. W. and M. R. Z. are grateful for the support from the Multidisciplinary University Research Initiative (MURI) grant.

References

1 B. Dunn, H. Kamath and J.-M. Tarascon, *Science*, 2011, **334**, 928–935.
2 D. Larcher and J.-M. Tarascon, *Nat. Chem.*, 2015, **7**, 19.
3 G. B. Haxel, J. B. Hedrick, G. J. Orris, P. H. Stauffer and J. W. Hendley II, Rare earth elements: critical resources for high technology, Report 2327-6932, 2002.
4 Y. Liang, Z. Chen, Y. Jing, Y. Rong, A. Facchetti and Y. Yao, *J. Am. Chem. Soc.*, 2015, **137**, 4956–4959.
5 N. Yabuuchi, K. Kubota, M. Dahbi and S. Komaba, *Chem. Rev.*, 2014, **114**, 11636–11682.
6 V. Mathew, S. Kim, J. Kang, J. Gim, J. Song, J. P. Baboo, W. Park, D. Ahn, J. Han and L. Gu, *NPG Asia Mater.*, 2014, **6**, e138.
7 N. Recham, G. l. Rousse, M. T. Sougrati, J.-N. l. Chotard, C. Frayret, S. Mariyappan, B. C. Melot, J.-C. Jumas and J.-M. Tarascon, *Chem. Mater.*, 2012, **24**, 4363–4370.
8 C. Zhang, Y. Xu, M. Zhou, L. Liang, H. Dong, M. Wu, Y. Yang and Y. Lei, *Adv. Funct. Mater.*, 2017, **27**, 1604307.
9 P. Padigi, J. Thiebes, M. Swan, G. Goncher, D. Evans and R. Solanki, *Electrochim. Acta*, 2015, **166**, 32–39.
10 Y. Chen, W. Luo, M. Carter, L. Zhou, J. Dai, K. Fu, S. Lacey, T. Li, J. Wan and X. Han, *Nano Energy*, 2015, **18**, 205–211.
11 J. Zelang, X. Zhenyu, B. Clement, L. Zhifei and J. Xiulei, *Adv. Energy Mater.*, 2016, **6**, 1501874.
12 Z. Tai, Q. Zhang, Y. Liu, H. Liu and S. Dou, *Carbon*, 2017, **123**, 54–61.
13 Z. Jian, W. Luo and X. Ji, *J. Am. Chem. Soc.*, 2015, **137**, 11566–11569.
14 S. Komaba, T. Hasegawa, M. Dahbi and K. Kubota, *Electrochem. Commun.*, 2015, **60**, 172–175.
15 W. Luo, J. Wan, B. Ozdemir, W. Bao, Y. Chen, J. Dai, H. Lin, Y. Xu, F. Gu and V. Barone, *Nano Lett.*, 2015, **15**, 7671–7677.
16 Y. Liang, H. Tian, J. Repac, S.-C. Liou, J. Chen, W. Han, C. Wang and S. Ehrman, *Energy Storage Mater.*, 2018, **13**, 8–18.
17 I. Sultana, T. Ramireddy, M. M. Rahman, Y. Chen and A. M. Glushenkov, *Chem. Commun.*, 2016, **52**, 9279–9282.
18 Z. Li, J. Ding and D. Mitlin, *Acc. Chem. Res.*, 2015, **48**, 1657–1665.
19 K. T. Lee, Y. S. Jung and S. M. Oh, *J. Am. Chem. Soc.*, 2003, **125**, 5652–5653.
20 H. Kim, G.-S. Park, E. Kim, J. Kim, S.-G. Doo and J. Cho, *J. Electrochem. Soc.*, 2006, **153**, A1633–A1636.
21 J. Yin, M. Wada, S. Tanase and T. Sakai, *J. Electrochem. Soc.*, 2004, **151**, A583–A589.
22 W.-J. Zhang, *J. Power Sources*, 2011, **196**, 13–24.
23 J. Qian, Y. Chen, L. Wu, Y. Cao, X. Ai and H. Yang, *Chem. Commun.*, 2012, **48**, 7070–7072.
24 J. Sangster and A. Pelton, *J. Phase Equilib.*, 1993, **14**, 514–517.
25 W. D. McCulloch, X. Ren, M. Yu, Z. Huang and Y. Wu, *ACS Appl. Mater. Interfaces*, 2015, **7**, 26158–26166.
26 D. Aurbach, *J. Power Sources*, 2000, **89**, 206–218.
27 Y. Lei, L. Qin, R. Liu, K. C. Lau, Y. Wu, D. Zhai, B. Li and F. Kang, *ACS Appl. Energy Mater.*, 2018, **1**, 1828–1833.
28 X. Wu, D. P. Leonard and X. Ji, *Chem. Mater.*, 2017, **29**, 5031–5042.
29 F. Su, X. Zhao, Y. Wang, J. Zeng, Z. Zhou and J. Y. Lee, *J. Phys. Chem. B*, 2005, **109**, 20200–20206.
30 H. Hou, M. Jing, Y. Yang, Y. Zhang, W. Song, X. Yang, J. Chen, Q. Chen and X. Ji, *J. Power Sources*, 2015, **284**, 227–235.
31 Y. Yang, M. Romano, G. Feng, X. Wang, T. Wu, S. Holdren and M. R. Zachariah, *Langmuir*, 2018, **34**, 585–594.
32 Z. Jian, Z. Xing, C. Bommier, Z. Li and X. Ji, *Adv. Energy Mater.*, 2016, **6**, 1501874.
33 A. Darwiche, C. Marino, M. T. Sougrati, B. Fraisse, L. Stievano and L. Monconduit, *J. Am. Chem. Soc.*, 2012, **134**, 20805–20811.
34 H. Hou, G. Zou, P. Ge, G. Zhao, W. Wei, X. Ji and L. Huang, *New J. Chem.*, 2017, **41**, 13724–13731.
35 W. Weppner and R. A. Huggins, *J. Electrochem. Soc.*, 1977, **124**, 1569–1578.
36 Y. Xu, C. Zhang, M. Zhou, Q. Fu, C. Zhao, M. Wu and Y. Lei, *Nat. Commun.*, 2018, **9**, 1720.
37 E. J. Ra, E. Raymundo-Piñero, Y. H. Lee and F. Béguin, *Carbon*, 2009, **47**, 2984–2992.
38 K. F. Chiu and P. Lai, *Mater. Sci. Eng., B*, 2018, **228**, 52–59.
39 X. B. Cheng, R. Zhang, C. Z. Zhao, F. Wei, J. G. Zhang and Q. Zhang, *Adv. Sci.*, 2016, **3**, 1500213.
40 C. Xu, B. Sun, T. Gustafsson, K. Edström, D. Brandell and M. Hahlin, *J. Mater. Chem. A*, 2014, **2**, 7256–7264.